

Lecture Series

Modern Methods in Heterogeneous Catalysis

Script to Lecture
Raman Spectroscopy

Raimund Horn

Fritz-Haber-Institute of the MPG
Department of Inorganic Chemistry
Faradayweg 4-6
14195 Berlin

Phone: 030 - 8413 - 4420

E-Mail: horn_r@fhi-berlin.mpg.de

23.01.2009

Contents

1	Introduction and Terminology	3
2	History of Raman Spectroscopy	4
3	Presentation of Raman Spectra	5
4	Theory of Rayleigh and Raman Scattering	5
4.1	Tools	8
4.1.1	Plane Wave	8
4.1.2	Polarizability Tensor	10
4.1.3	Normal Vibrations	12
4.1.4	Taylor Series	14
4.2	Classical Theory	14
4.2.1	Selection Rules	16
4.2.2	Limitations of the Classical Theory	17
4.3	Quantum Mechanical Theory	21
4.3.1	Frequency denominators	21
4.3.2	Transition electric dipole numerators	22
5	Instrumentation	24
5.1	Laser	25
5.2	Sample Illumination	27
5.3	Analysis of the Scattered Light	27
5.3.1	Dispersive Spectrometer	27
5.3.2	Laser Line Rejection	32
5.3.3	Detector	33
5.4	Raman Microscopy	35
6	Application of Raman Spectroscopy in Catalysis	38
6.1	General Comments	38
6.2	Example: Mechanism of NO_2 storage on BaO supported on MgO	39

1 Introduction and Terminology

When monochromatic radiation of frequency ω_1 is incident on ideal systems (dust-free transparent gases and liquids, transparent solids etc.), most of it is transmitted without change, only a small amount is scattered. Scattering means, the light deviates from its original straight trajectory (Figure 1). If the frequency content of the scattered light is analyzed it turns out that most of the scattered light is scattered elastically (Rayleigh Scattering), i.e. $\omega_s = \omega_1$ but also, that a tiny amount is scattered inelastically $\omega_s = \omega_1 \pm \omega_M$ (Raman Scattering).

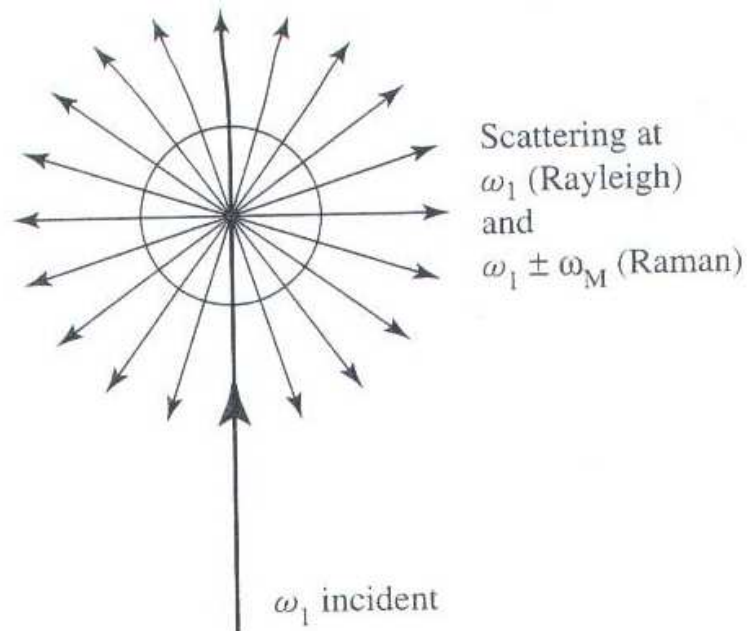


Figure 1: Schematic illustration of light scattering. Adopted from [1]

In the inelastic scattering event energy is transferred between the scattered photon and a rotational or vibrational state of the molecule or a phonon in the crystal lattice. Raman bands at frequencies less than the incident frequency $\omega_1 - \omega_M$ are referred to as Stokes bands and those at higher frequencies $\omega_1 + \omega_M$ are called anti-Stokes bands. Typically the intensity of the Rayleigh line is a factor of 10^{-3} lower than the intensity of the incident excitation and the Raman lines are another factor of 10^{-3} weaker ($I_{Raman} \approx 10^{-3} I_{Rayleigh} \approx 10^{-6} I_{in}$).

2 History of Raman Spectroscopy

Elastic light scattering has been observed since the 19th century by famous physicists like Lord Rayleigh or Albert Einstein. However, apart from Compton Scattering in the X-Ray and Gamma region of the electromagnetic spectrum, no inelastic scattering had been observed experimentally, even though the effect had been predicted theoretically by A. Smekal in 1923 [2]. The first experimental observation of inelastic light scattering by molecules in liquid phase was made by Chandrasekhara Raman (Figure 2) and his student Kariamanikkam Srinivasa Krishnan in 1928 [3, 4]. Essentially simultaneously, G. Landsberg and L. Mandelstam dis-



Figure 2: Chandrashekara Venkata Raman (1888-1970)

covered the same effect in crystals [5]. In 1930, C.V. Raman received the Nobel Prize in Physics for this discovery and the Raman effect carries his name ever since.

Despite the initial excitement about the discovery of the Raman effect, its spectroscopic application remained quite limited until 1960 when the first laser was developed by T. Maiman. Before the advent of the laser, which is due to its brilliance, monochromaticity and coherence the ideal excitation source for light scattering experiments, Raman Spectroscopy suffered from the low intensity of the inelastic scattering and the much larger intensity of the Rayleigh scattering.

3 Presentation of Raman Spectra

The use of the angular frequency $\omega = 2\pi\nu = 2\pi\frac{c_0}{\lambda}$ is very convenient for theoretical treatments but uncommon in the representation of spectra. Spectra are usually displayed on a wavenumber scale ($\tilde{\nu}_M$ unit cm^{-1}) which is related to ω_M by $\tilde{\nu}_M = \omega_M/2\pi c_0$. Figures 3a) and b) show facsimiles of photographically recorded spectra of CCl_4 reported by Raman and Krishnan [6] using a mercury arc as excitation source (435.83 nm , $\tilde{\nu}_1 = 22938\text{ cm}^{-1}$) and Figure 3c) shows the spectrum excited by an Ar^+ laser (487.99 nm , $\tilde{\nu}_1 = 20487\text{ cm}^{-1}$) and recorded directly. A Raman spectrum of CCl_4 presented according to the recommendations of the IUPAC is shown in Figure 4.

4 Theory of Rayleigh and Raman Scattering

The phenomenon of light scattering can be described either classically or quantum mechanically by perturbation theory. Either way, the origin of the scattered radiation is considered to be the oscillating electric and magnetic multipole moments induced in a molecule by the electromagnetic fields of the incident light waves. For normal Raman spectroscopy, the important multipole source is the oscillating electric dipole. For that reason we will limit our discussion to the electric dipole. Theoretical aspects of light scattering by oscillating magnetic dipoles

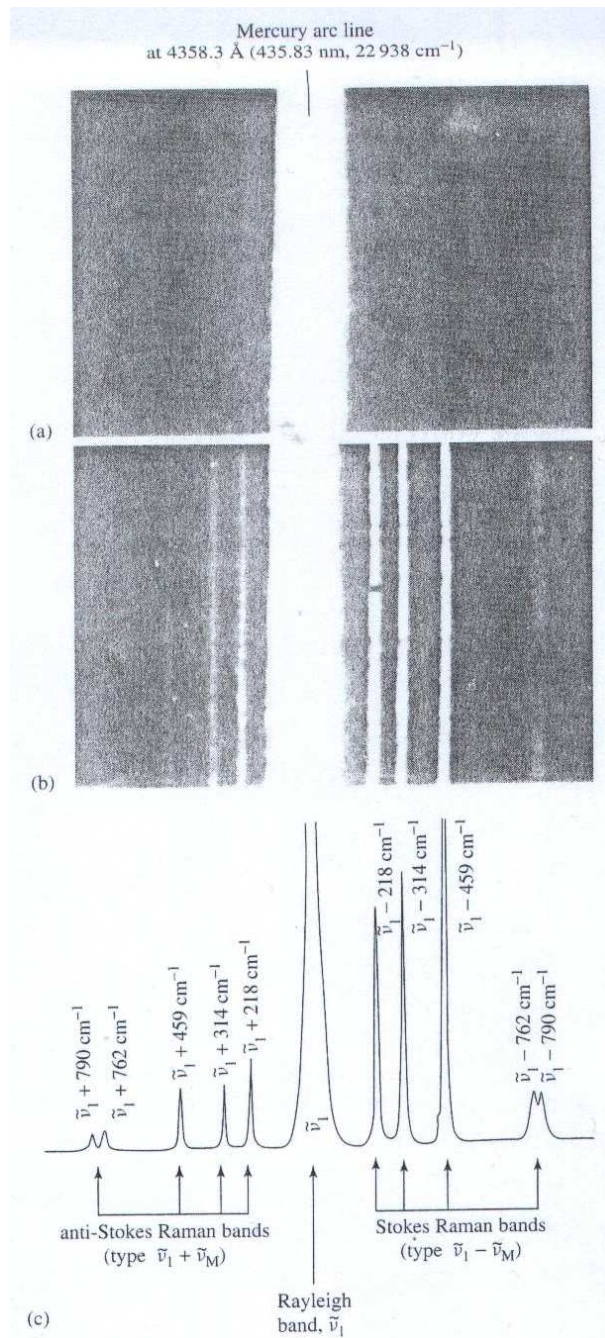


Figure 3: (a) Spectrum of a mercury arc in the region of 4358.3 Å (435.83 nm, $\tilde{\nu}_1 = 22938 \text{ cm}^{-1}$). (b) Rayleigh and Raman Spectra of CCl_4 excited by mercury arc radiation at $\tilde{\nu}_1 = 22938 \text{ cm}^{-1}$. (c) Rayleigh and Raman spectra of CCl_4 excited by an Ar^+ laser $\tilde{\nu}_1 = 20487 \text{ cm}^{-1}$ (487.99 nm). Adopted from [1]

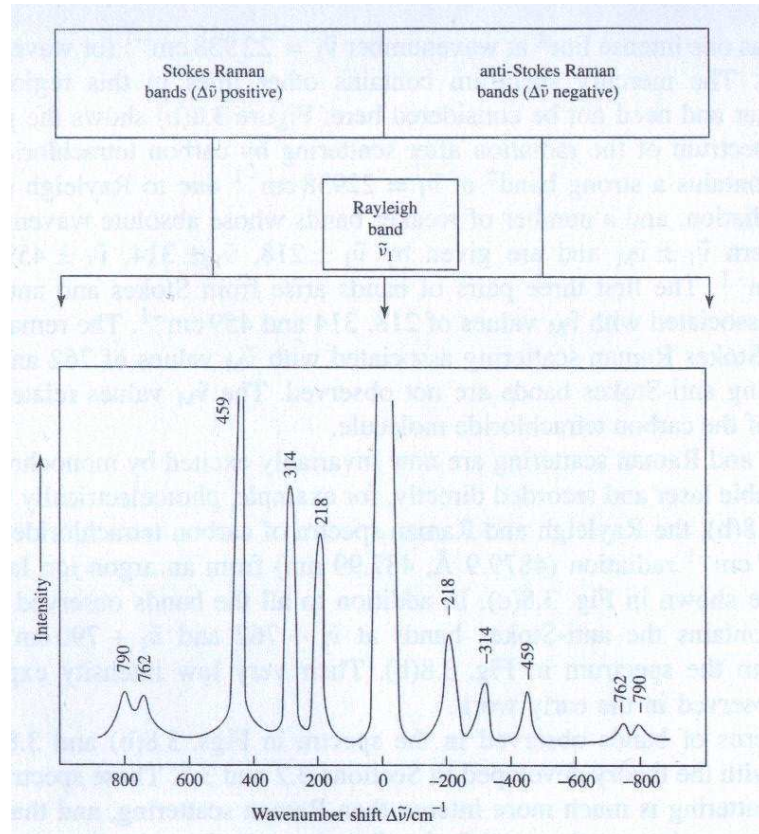


Figure 4: Presentation of the Raman spectrum of CCl_4 according to IUPAC recommendation

and electric quadrupoles can be found in [1].

The intensity I , the time-averaged power per unit solid angle (what your detector measures), radiated by an oscillating electric dipole induced in a molecule by the electric field of the incident radiation of frequency ω_1 , along a direction making an angle θ with the axis of the dipole is given by Eqn. 1 with the constant k'_ω give by Eqn. 2

$$I = k'_\omega \omega_s^4 p_0^2 \sin^2 \theta \quad (1)$$

$$k'_\omega = \frac{1}{32\pi^2 \epsilon_0 c_0^3} \quad (2)$$

p_0 is the amplitude of the induced oscillating electric dipole with frequency ω_s which is for Rayleigh scattering equal to ω_1 but for Raman scattering different from ω_1 . Objective of both the classical and quantum mechanical treatments of light scattering is to find how ω_s and p_0 are determined by the properties of the scattering molecule and the incident electromagnetic radiation of frequency ω_1 .

4.1 Tools

4.1.1 Plane Wave

The propagation of an unattenuated wave through an isotropic medium with speed v is generally described by the Helmholtz Equation 3.

$$\nabla^2 \Psi = \frac{1}{v^2} \frac{\partial^2 \Psi}{\partial t^2} \quad (3)$$

The propagated quantity Ψ can either be a scalar or a vector. For an electromagnetic wave with \mathbf{E} as the electric field strength and \mathbf{B} the magnetic flux density, Eqn. 3 takes the form 4 and 5 respectively, with c_0 being the speed of light in vacuum.

$$\nabla^2 \mathbf{E} = \frac{1}{c_0^2} \frac{\partial^2 \mathbf{E}}{\partial t^2} \quad (4)$$

$$\nabla^2 \mathbf{B} = \frac{1}{c_0^2} \frac{\partial^2 \mathbf{B}}{\partial t^2} \quad (5)$$

There are many solutions to Eq. 4 but for light scattering the special case of a monochromatic, plane, harmonic, electromagnetic wave propagating along one distinct direction is of particular importance.

Such a plane wave has the property that for any plane normal to the direction of propagation, the quantity being propagated has the same value over that plane at a given time. Therefore, the vector \mathbf{E} is constant over the x, y plane.

$$\mathbf{E} = \mathbf{e}_x E_x + \mathbf{e}_y E_y \quad (6)$$

The solution of Eqn. 4 for a plane wave which is harmonic in time and monochromatic is given by

$$\mathbf{E} = \mathbf{E}_0 \cos \left\{ \omega \left(t - \frac{z}{c_0} \right) + \theta \right\} \quad (7)$$

To simplify things, we set $E_{y_0} = 0$ so that $\mathbf{E} = \mathbf{e}_x E_x$ and $\mathbf{E}_0 = \mathbf{e}_x E_{x_0}$ which leads for propagation along the positive z axis to

$$E_x = E_{x_0} \cos \left\{ \omega \left(t + \frac{z}{c_0} \right) + \theta \right\} \quad (8)$$

The treatment for the magnetic flux density \mathbf{B} is analogue with the only requirement that:

$$\mathbf{B} = \frac{1}{c_0} [\mathbf{e}_z \times \mathbf{E}] \quad (9)$$

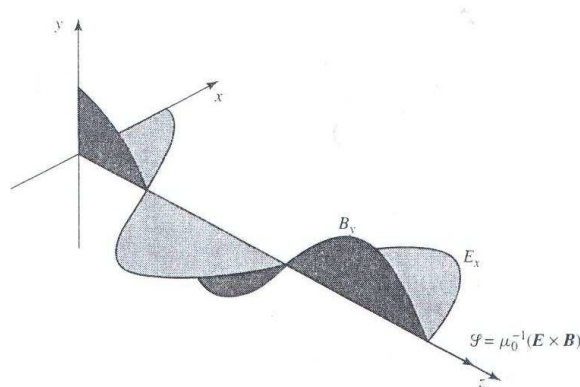


Figure 5: Variation of $\mathbf{E} = e_x E_x$ and $\mathbf{B} = e_y B_y$ with z at a particular instant for a plane electromagnetic wave travelling along the z axis ($\mathbf{n}_0 = e_z$).

The variation of \mathbf{E} and \mathbf{B} with z at constant t is shown in Figure 5. A plane wave is described by a number of important properties:

- E_{x0} , the amplitude of the electromagnetic wave, is always greater than zero and the maximum value E_x can take
- the angular frequency $\omega = 2\pi\nu$ specifies what angle the wave covers per second and is related to ν by $\omega = 2\pi\nu$
- E_x remains unchanged in magnitude when t is replaced by $t + T$, where T , the period, is defined by $T = 1/\nu = 2\pi/\omega$
- E_x remains also unchanged in magnitude when z is replaced by $z + \lambda_0$ where $\lambda_0 = c_0/\nu = 2\pi c_0/\omega = c_0 T$ is called the wavelength of the wave in vacuum
- the number of wavelengths per unit length in vacuum is the wavenumber $\tilde{\nu}$ and thus $\tilde{\nu} = 1/\lambda_0$ which is preferentially used in units of cm^{-1} . The wavenumber and the angular frequency are connected by $\omega = 2\pi c_0 \tilde{\nu}$

To characterize the propagation direction and the angle covered by propagation into this direction the wave vector \mathbf{k}_0 is defined

$$\mathbf{k}_0 = k_0 \mathbf{n}_0 \quad (10)$$

The direction of the wave vector \mathbf{k}_0 is specified by the unit vector \mathbf{n}_0 and the amplitude is give by the scalar quantity

$$k_0 = \frac{2\pi}{\lambda_0} = \frac{2\pi\nu}{c_0} = \frac{\omega}{c_0} \quad (11)$$

The equation of a plane perpendicular to \mathbf{k}_0 is

$$\mathbf{k}_0 \cdot \mathbf{r} = \text{constant} \quad (12)$$

Consequently, an equation of the form

$$\Psi(\mathbf{r}) = \mathbf{A} \cos(\mathbf{k}_0 \cdot \mathbf{r}) \quad (13)$$

in which \mathbf{A} is the amplitude of $\Psi(\mathbf{r})$ represents a set of planes over which $\Psi(\mathbf{r})$ varies in space sinusoidally. This behavior is illustrated in Fig. 6. If Eqn. 13 is now combined with a sinusoidal time function $\cos(\omega t)$ and \mathbf{A} is set to be the electric field vector, the electric field vector \mathbf{E} of a plane wave can be computed at any position \mathbf{r} and at any time t :

$$\mathbf{E} = \mathbf{E}_0 \cos(\omega t - \mathbf{k}_0 \cdot \mathbf{r}) \quad (14)$$

4.1.2 Polarizability Tensor

The frequency dependent induced electric dipole vector \mathbf{p} for a molecule under influence of the electric field vector \mathbf{E} is given by Eqn. 15

$$\mathbf{p} = \boldsymbol{\alpha} \cdot \mathbf{E} \quad (15)$$

In Eqn. 15, \mathbf{E} is the electric field vector of the incident, plane wave, monochromatic radiation of frequency ω_1 and $\boldsymbol{\alpha}$ is the polarizability tensor of the molecule.

Eq. 15 implies that the magnitudes of the components of \mathbf{P} are related to the magnitudes of the components of \mathbf{E} by the following three linear equations:

$$P_x = \alpha_{xx}E_x + \alpha_{xy}E_y + \alpha_{xz}E_z \quad (16)$$

$$P_y = \alpha_{yx}E_x + \alpha_{yy}E_y + \alpha_{yz}E_z \quad (17)$$

$$P_z = \alpha_{zx}E_x + \alpha_{zy}E_y + \alpha_{zz}E_z \quad (18)$$

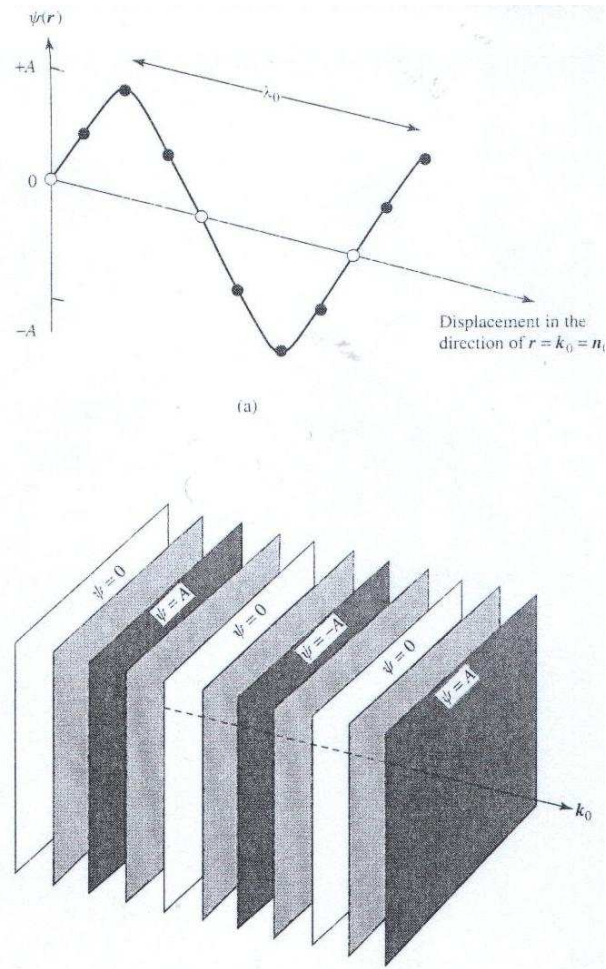


Figure 6: The function $\Psi(\mathbf{r}) = A \cos(\mathbf{k}_0 \cdot \mathbf{r})$.

The nine coefficients α_{ij} are called the components of the polarizability tensor α . Since α is real and symmetric, i.e. $\alpha_{xy} = \alpha_{yx}$, $\alpha_{xz} = \alpha_{zx}$ and $\alpha_{yz} = \alpha_{zy}$ the tensor has a maximum of six distinct components, all of which are real. The components of α will generally change with the choice of the coordinate system, however, the magnitudes and directions of the \mathbf{E} and \mathbf{P} vectors can not change.

It is obvious from Eq. 16, that the direction of the induced dipole will usually be different from that of the electric field, since each component is determined from all three components of \mathbf{E} . Even if there is only one component of \mathbf{E} , it is possible to produce three components of \mathbf{P} as shown in Figure 7.

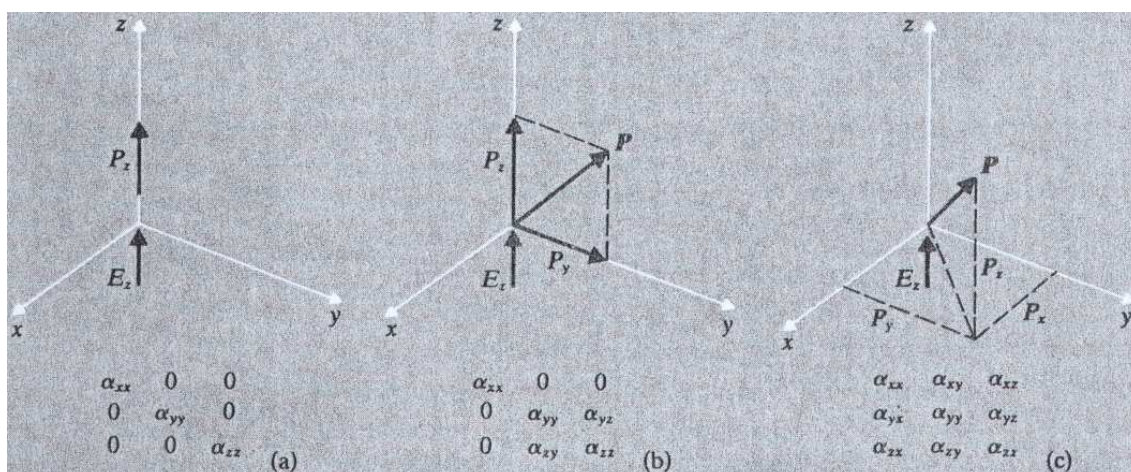


Figure 7: Dependence of the direction of the induced dipole \mathbf{P} on the form of the polarizability tensor: (a) diagonal tensor ($\alpha_{ij} = 0$); (b) $\alpha_{xy} = \alpha_{xz} = 0$; (c) no non-zero components. Adopted from [7]

4.1.3 Normal Vibrations

The vibration of molecules can be described by a limited number of fundamental motions called *normal modes of vibration*. Normal modes fulfill the following criteria:

- each atom oscillates in a normal mode about its equilibrium position with a simple harmonic motion of a certain amplitude, frequency and phase
- in a given normal mode all atoms oscillate with the same frequency and phase, i.e. they reach their maximum and minimum position at the same time
- the center of mass of the molecule does not change during a normal mode
- normal modes are independent and can be excited independently
- a linear molecule has $3N - 5$, a nonlinear molecule has $3N - 6$ normal modes

For illustration Figure 8 shows the normal modes of B_2H_6 .

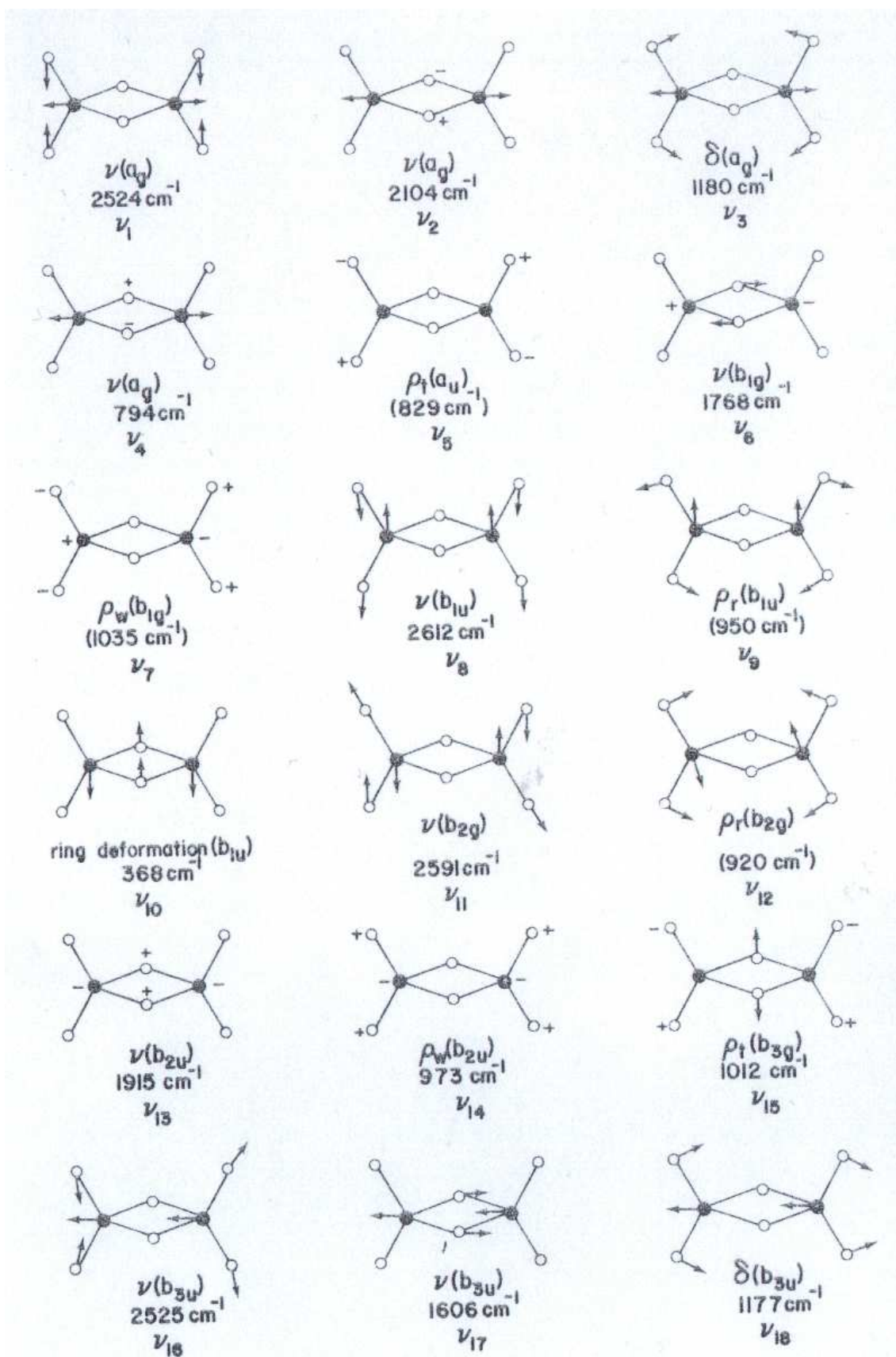


Figure 8: Normal modes of vibration of B_2H_6 . Adopted from [8]

4.1.4 Taylor Series

The last tool we need for the classical description of the Raman effect are Taylor Series. Taylor Series are used in Physics to approximate a complex function f around a point a by a power series which can be truncated after a few terms still giving a good approximation to the function f .

$$f(x) = \sum_{n=0}^{\infty} \frac{f^{(n)}(a)}{n!} (x - a)^n \quad (19)$$

As example, Eq. 20 and Fig. 9 show the development of the $\sin(x)$ function around $a = 0$ in a Taylor Series.

$$\sin(x) = \sum_{n=0}^{\infty} (-1)^n \frac{x^{2n+1}}{(2n+1)!} \quad (20)$$

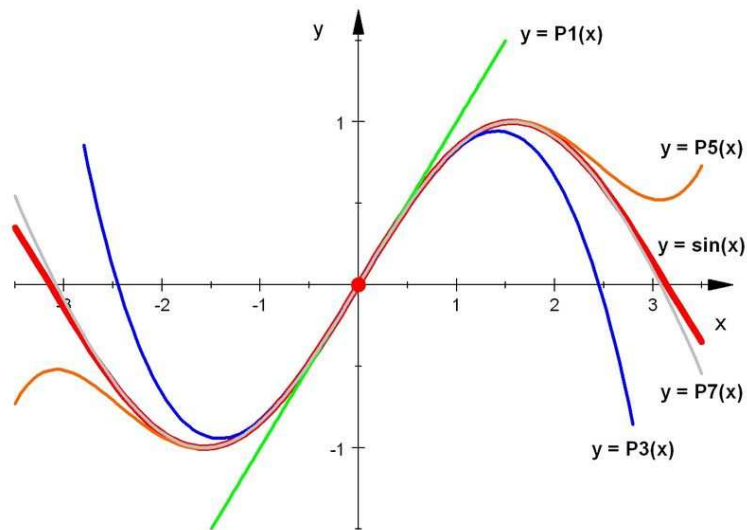


Figure 9: Taylor approximation of $\sin(x)$, Source: Wikipedia

4.2 Classical Theory

Objective of the classical theory is to calculate for a molecule the frequency-dependent linear induced electric dipole vectors $\mathbf{p}^{(1)}$ making use of the relationship

$$\mathbf{p}^{(1)} = \boldsymbol{\alpha} \cdot \mathbf{E} \quad (21)$$

The polarizability tensor will, in general, be a function of the nuclear coordinates and hence of the molecular vibrational frequencies. Therefore, the frequency dependent induced electric dipole vectors $\mathbf{p}^{(1)}$ will be obtained by introducing into Eqn. 21 the frequency dependence of \mathbf{E} and α . The amplitude of a linear induced electric dipole of a particular frequency enables the scattered intensity to be calculated using Eqn. 1. To make life easier, the scattering system is assumed to be a molecule which is free to vibrate but is fixed in space and can not rotate.

The variation of the polarizability with vibrations of the molecule can be expressed by expanding each component of $\alpha_{\rho\sigma}$ in a Taylor series with respect to the normal coordinates around the equilibrium configuration (index 0):

$$\alpha_{\rho\sigma} = (\alpha_{\rho\sigma})_0 + \sum_k \left(\frac{\partial \alpha_{\rho\sigma}}{\partial Q_k} \right)_0 Q_k + \frac{1}{2} \sum_{k,l} \left(\frac{\partial^2 \alpha_{\rho\sigma}}{\partial Q_k \partial Q_l} \right)_0 Q_k Q_l \dots \quad (22)$$

In good approximation, powers of Q higher than the first can be omitted and if we restrict ourself initially to one normal mode of vibration Q_k , Eq. 22 simplifies to 23 or in vector notation to 24

$$(\alpha_{\rho\sigma})_k = (\alpha_{\rho\sigma})_0 + (\alpha'_{\rho\sigma})_k Q_k \quad (23)$$

$$\boldsymbol{\alpha}_k = \boldsymbol{\alpha}_0 + \boldsymbol{\alpha}'_k Q_k \quad (24)$$

Assuming simple harmonic motion, the time dependence of Q_k is given by

$$Q_k = Q_{k0} \cos(\omega_k t + \delta_k) \quad (25)$$

Combining Eq. 24 with Eq. 25 leads to the time dependence of the polarizability tensor resulting from the k th molecular vibration:

$$\boldsymbol{\alpha}_k = \boldsymbol{\alpha}_0 + \boldsymbol{\alpha}'_k Q_{k0} \cos(\omega_k t + \delta_k) \quad (26)$$

If we insert the frequency dependence of $\boldsymbol{\alpha}_k$ (Eq. 26) and $\mathbf{E} = \mathbf{E}_0 \cos(\omega_1 t)$ into Eq. 21 we obtain

$$\mathbf{p}^{(1)} = \boldsymbol{\alpha}_0 \mathbf{E}_0 \cos(\omega_1 t) + \boldsymbol{\alpha}'_k \mathbf{E}_0 Q_{k0} \cos(\omega_1 t) \cos(\omega_k t + \delta) \quad (27)$$

Using the trigonometric identity

$$\cos(A)\cos(B) = \frac{1}{2} \{ \cos(A+B) + \cos(A-B) \} \quad (28)$$

we obtain the final result

$$\mathbf{p}^{(1)} = \mathbf{p}^{(1)}(\omega_1) + \mathbf{p}^{(1)}(\omega_1 - \omega_k) + \mathbf{p}^{(1)}(\omega_1 + \omega_k) \quad (29)$$

$$\mathbf{p}^{(1)}(\omega_1) = \mathbf{p}_0^{\text{Ray}} \cos(\omega_1 t) \quad (30)$$

$$\mathbf{p}_0^{\text{Ray}} = \boldsymbol{\alpha}^{\text{Ray}} \cdot \mathbf{E}_0 = \boldsymbol{\alpha}_0 \cdot \mathbf{E}_0 \quad (31)$$

$$\mathbf{p}^{(1)}(\omega_1 \pm \omega_k) = \mathbf{p}_{k_0}^{\text{Ram}} \cos((\omega_1 \pm \omega_k \pm \delta_k)t) \quad (32)$$

$$\mathbf{p}_{k_0}^{\text{Ram}} = \boldsymbol{\alpha}_k^{\text{Ram}} \cdot \mathbf{E}_0 \quad (33)$$

$$\boldsymbol{\alpha}_k^{\text{Ram}} = \frac{1}{2} \boldsymbol{\alpha}'_k Q_k \quad (34)$$

Eq. 29 shows that the linear induced dipole has three distinct frequency components: $\mathbf{p}^{(1)}(\omega_1)$ which gives rise to radiation at ω_1 and so accounts for Rayleigh scattering; $\mathbf{p}^{(1)}(\omega_1 - \omega_k)$ which gives rise to radiation at $\omega_1 - \omega_k$ and so accounts for Stokes Raman scattering and finally $\mathbf{p}^{(1)}(\omega_1 + \omega_k)$ which gives rise to radiation at $\omega_1 + \omega_k$ and so accounts for Anti-Stokes Raman scattering (Figure 10). It should be noted here that the induced dipole $\mathbf{p}^{(1)}(\omega_1)$ is in phase with the incident radiation whereas the induced dipoles oscillating at frequencies $\omega_1 \pm \omega_k$ are phase shifted by δ_k relative to the incident field. In practice that means, that Rayleigh scattering might not scale linearly with the scatterer density. For Raman scattering every molecule acts as independent source of radiation and the total scattered intensity scales linearly with the number of scatterers (important for quantitative analysis!!!).

4.2.1 Selection Rules

It is evident from Eq. 31 that Rayleigh scattering occurs if $\boldsymbol{\alpha}^{\text{Ray}}$ is non zero. As the electron clouds of all molecules are polarizable to a greater or lesser extent, $\boldsymbol{\alpha}^{\text{Ray}}$ will always have some non-zero components and Rayleigh scattering will always occur.

According to Eq. 34 the necessary condition for Raman scattering associated with a molecular frequency ω_k is that $\boldsymbol{\alpha}^{\text{Ram}}$ has at least one component ($\partial\alpha_{\rho\sigma}/\partial Q_k$) that is non-zero. Figures 11-13 illustrate this selection rule for the simple cases of a linear diatomic molecule, a linear triatomic molecule and an angular triatomic

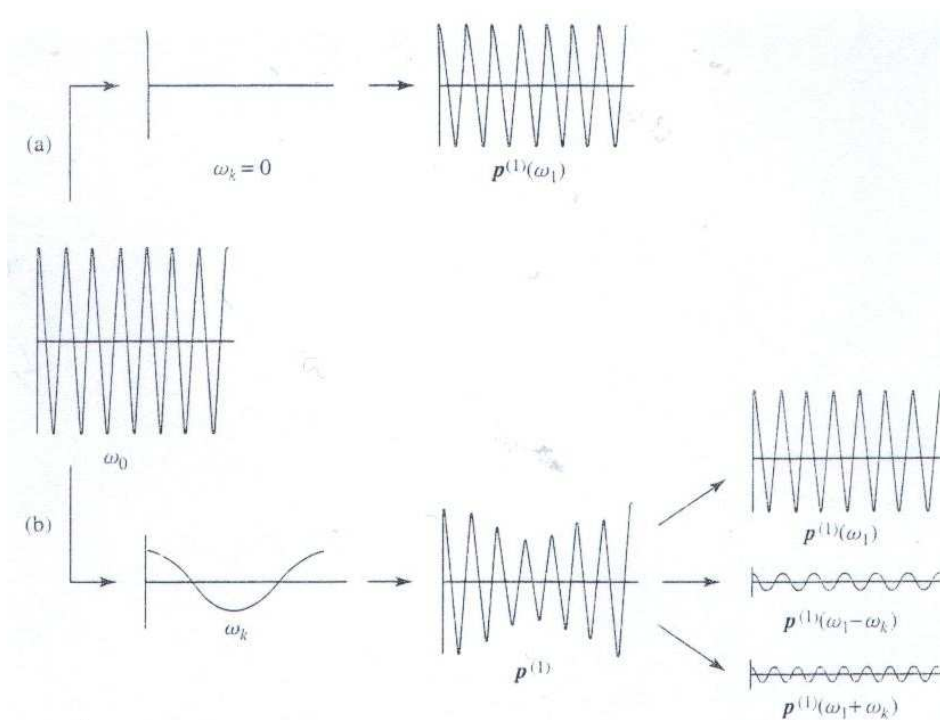


Figure 10: Time dependence of the linear induced dipoles $\mathbf{p}^{(1)}$ produced by electromagnetic radiation of frequency ω_1 : (a) scattering molecule not vibrating $\omega_k = 0$: $\mathbf{p}^{(1)} = \mathbf{p}^{(1)}(\omega_1)$; (b) scattering molecule vibrating with frequency ω_k : $\mathbf{p}^{(1)} = \mathbf{p}^{(1)}(\omega_1) + \mathbf{p}^{(1)}(\omega_1 - \omega_k) + \mathbf{p}^{(1)}(\omega_1 + \omega_k)$

molecule respectively and compares to the selection rule of infrared activity which is that the dipole moment changes by the vibration.

4.2.2 Limitations of the Classical Theory

- no description of molecular rotation
- vibrational Raman scattering tensor only partly correct
- no information how α'_k depends on the characteristic transition frequencies of the molecule (resonance Raman effect)

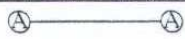
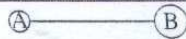

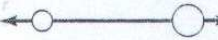
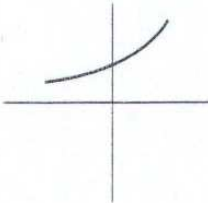
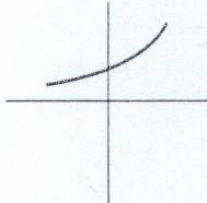
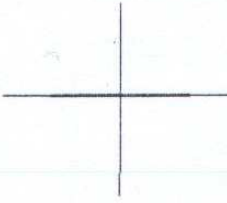
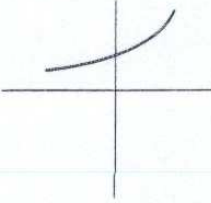
Molecule		
Mode of vibration		
Variation of polarizability with normal coordinate (schematic)		
Polarizability derivative at equilibrium position	$\neq 0$	$\neq 0$
Raman activity	Yes	Yes
Variation of dipole moment with normal coordinate (schematic)		
Dipole moment derivative at equilibrium position	$= 0$	$\neq 0$
Infrared activity	No	Yes

Figure 11: Comparison of polarizability and dipole moment variations in the neighbourhood of the equilibrium position and vibrational Raman and infrared activities for an A_2 and an AB molecule. Adopted from [1]

Molecule			
Mode of vibration			
Variation of polarizability with normal coordinate (schematic)			
Polarizability derivative at equilibrium position	$\neq 0$	$= 0$	$= 0$
Raman activity	Yes	No	No
Variation of dipole moment with normal coordinate (schematic)			
Dipole moment derivative at equilibrium position	$= 0$	$\neq 0$	$\neq 0$
Infrared activity	No	Yes	Yes

Figure 12: Polarizability and dipole moment variations in the neighbourhood of the equilibrium position and vibrational Raman and infrared activities for a linear *ABA* molecule. Adopted from [1]

Molecule			
Mode of vibration			
Variation of polarizability with normal coordinate (schematic)			
Polarizability derivative at equilibrium position	$\neq 0$	$\neq 0$	$\neq 0$
Raman activity	Yes	Yes	Yes
Variation of dipole moment with normal coordinate (schematic)			
Dipole moment derivative at equilibrium position	$\neq 0$	$\neq 0$	$\neq 0$
Infrared activity	Yes	Yes	Yes

Figure 13: Polarizability and dipole moment variations in the neighbourhood of the equilibrium position and vibrational Raman and infrared activities for a non-linear $A - B - A$ molecule. Adopted from [1]

4.3 Quantum Mechanical Theory

Goal of the quantum mechanical treatment of the Raman effect is to obtain expressions for the first order induced transition electric dipole moment $(\mathbf{p}^{(1)})_{fi}$ and hence the transition polarizability $(\alpha)_{fi}$. The treatment is based on time-dependent perturbation theory considering the incident electromagnetic wave as time dependent perturbation of the scatterer. As the quantum mechanical theory of Rayleigh and Raman scattering is beyond the scope of this script; the interested reader is referred to [1] for details. However, a qualitative discussion of the resulting equations (Eq. 35 and 36) will sensitize the user of Raman spectroscopy to advanced applications exploiting resonance Raman effects.

$$(p_{\rho}^{(1)})_{fi} = \frac{1}{2\hbar} \sum_{r \neq i, f} \left\{ \frac{\langle f | \hat{p}_{\rho} | r \rangle \langle r | \hat{p}_{\sigma} | i \rangle}{\omega_{ri} - \omega_1 - i\Gamma_r} + \frac{\langle f | \hat{p}_{\sigma} | r \rangle \langle r | \hat{p}_{\rho} | i \rangle}{\omega_{rf} + \omega_1 + i\Gamma_r} \right\} \tilde{E}_{\sigma_0} \exp(-i\omega_s t) \quad (35)$$

+ complex conjugate

$$(\alpha_{\rho\sigma})_{fi} = \frac{1}{2\hbar} \sum_{r \neq i, f} \left\{ \frac{\langle f | \hat{p}_{\rho} | r \rangle \langle r | \hat{p}_{\sigma} | i \rangle}{\omega_{ri} - \omega_1 - i\Gamma_r} + \frac{\langle f | \hat{p}_{\sigma} | r \rangle \langle r | \hat{p}_{\rho} | i \rangle}{\omega_{rf} + \omega_1 + i\Gamma_r} \right\} \quad (36)$$

4.3.1 Frequency denominators

The frequency denominators $(\omega_{ri} - \omega_1 - i\Gamma_r)$ of the first term in Eq. 35 involves differences of the type $\omega_{ri} - \omega_1$. In the case of normal Raman scattering (see Fig. 14) $\omega_1 \ll \omega_{ri}$ and $(\alpha_{\rho\sigma})_{fi}$ will take typical values. However, if ω_1 approaches or matches one or more particular absorption frequencies of the molecule ω_{ri} , $\omega_{ri} - \omega_1$ approaches zero and the term will tend to $-i\Gamma_r$. If the lifetime of the state $|r\rangle$ is not too short, the width of the level $|r\rangle$ Γ_r is small and $(p_{\rho}^{(1)})_{fi}$ can take extraordinary values, $10^3 - 10^6$ higher than for normal Raman scattering. This situation is called resonance Raman scattering. Figure 14 illustrates the different types of Raman scattering. In resonance Raman scattering, intensities of vibrations which are involved in the excited electronic transitions can be expected to be orders of magnitude larger than in normal Raman scattering. In some cases where $|r\rangle$ is short-lived (adsorbed species) Γ_r is large and resonance enhancement is not observed. Additionally, the relative position of the exciting frequency and the ab-

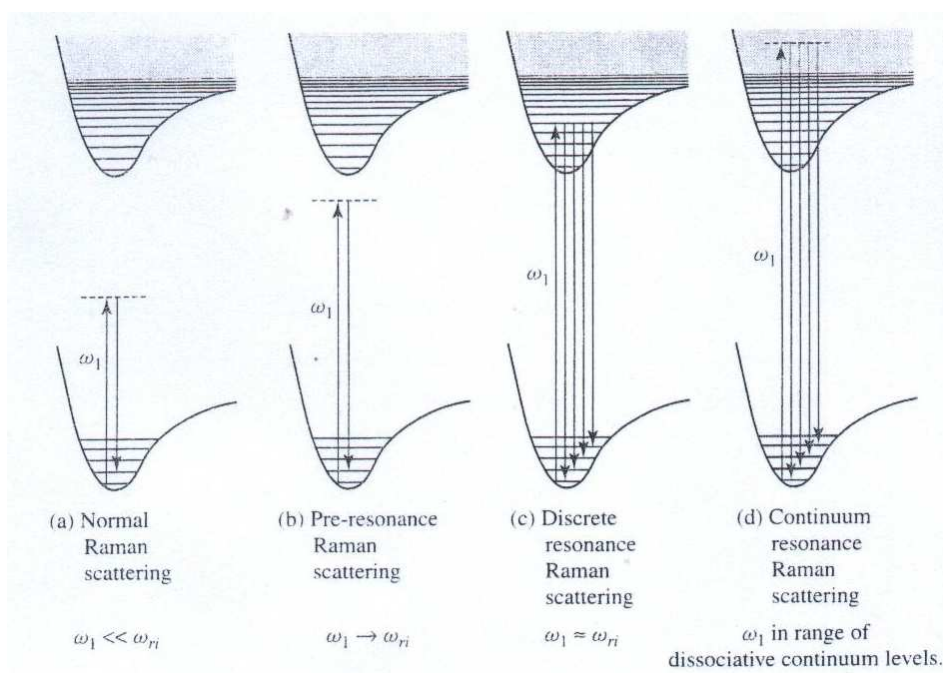


Figure 14: Four types of Raman scattering processes. Adopted from [1]

sorption band determines whether resonance enhancement is observed or not as the laser light can be absorbed or the scattered light can be re-adsorbed (Figure 15). Therefore, caution is advised in comparing Raman spectra measured at different wavelengths and a UV/Vis spectrum might be very helpful in interpreting resonance Raman effects. Figure 16 shows how resonance Raman scattering can be used to study partially reduced and defect rich MoO_{3-x} catalysts.

4.3.2 Transition electric dipole numerators

The transition electric dipole numerators in Eq. 35 are of the type $\langle f | \hat{p}_\rho | r \rangle \langle r | \hat{p}_\sigma | i \rangle$ and are hence the product of two transition electric dipole terms, one from state $|i\rangle$ to state $|r\rangle$ and one from state $|r\rangle$ to state $|f\rangle$. For normal Raman scattering ($\omega_1 \ll \omega_{ri}$) no terms dominate in Eq. 35 and all states $|r\rangle$ connecting the initial state $|i\rangle$ with the final state $|f\rangle$ contribute to the Raman signal. Therefore, normal Raman scattering is a ground state property and can only provide information about the ground vibronic and rovibronic states $|i\rangle$ and $|f\rangle$. In contrast, for resonance Raman scattering, the states $|r\rangle$ for which $\omega_1 \approx \omega_{ri}$ will predominate in

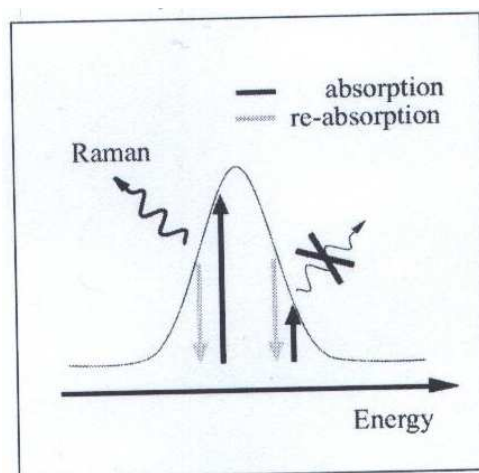


Figure 15: The exact position of the excitation wavelength and the wavelength of the emitted Raman light with respect to the electronic absorption determines the overall efficiency of the Raman scattering process. Adopted from [9]

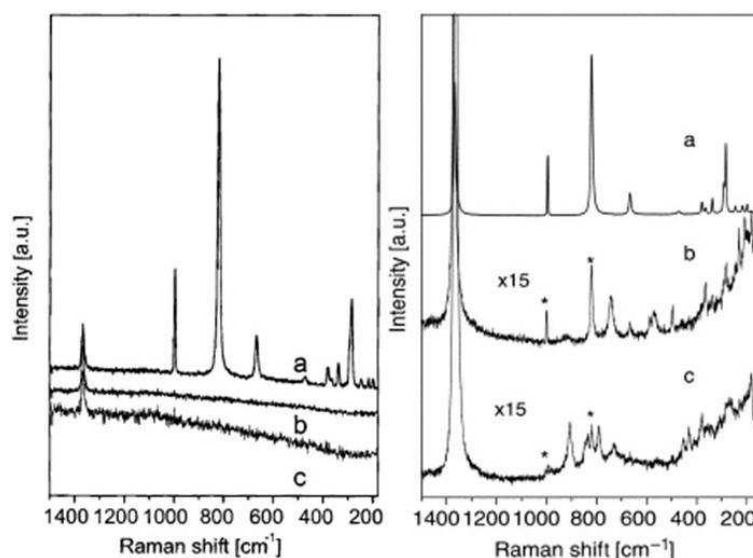


Figure 16: Characteristic Raman spectra taken of a boron nitride diluted sample of partially reduced MoO_{3-x} catalysts. Left panel $\lambda_1 = 532 \text{ nm}$; Right panel $\lambda_1 = 632.8 \text{ nm}$. a) MoO_3 , b) MoO_2 , c) Mo_4O_{11} . Adopted from [9]

the sum over the states $|r\rangle$ and $(\alpha_{\rho\sigma})_{fi}$ will be determined by the properties of a limited number of states $|r\rangle$, in lucky cases just by one. Therefore, resonance Raman scattering can provide detailed information about excited vibrational and rovibrational states.

The transition electric dipole numerators, specifically the vanishing of the integrals in the product terms $\langle f|\hat{p}_\rho|r\rangle\langle r|\hat{p}_\sigma|i\rangle$ determine also the selection rules in vibrational, rotational and ro-vibrational Raman scattering. For example, in vibrational Raman scattering, the condition that the xy component of α_{fi} , $(\alpha_{xy})_{fi}$ is non zero is, that the symmetry of the vibration is the same as one of the quadratic forms $xy, x^2 \dots$.

5 Instrumentation

The block diagram shown in Fig. 17 shows the components of the equipment necessary for Raman spectroscopy. In the Inorganic Chemistry Department, only

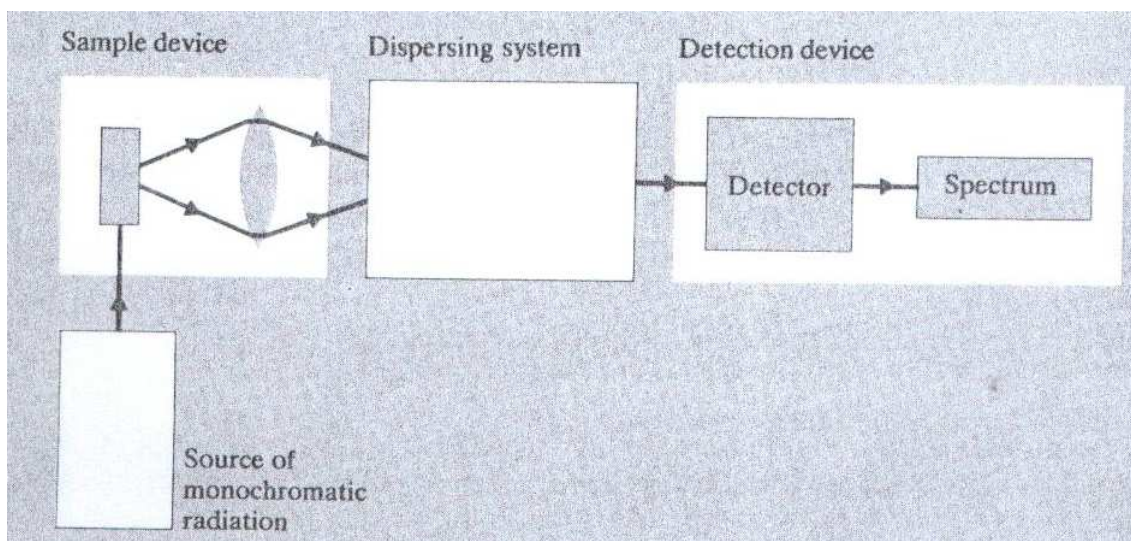


Figure 17: Necessary components to measure Raman spectra. Adopted from [7]

dispersive instruments using diffraction gratings and visible or UV excitation are used and will be discussed hereafter. A description of instruments for routine analysis employing near infrared lasers, interferometers and Fourier transformation for spectral analysis can be found elsewhere (e.g. [10]).

5.1 Laser

As already mentioned in the introduction, lasers are the ideal light source for Raman spectroscopy. Mercury arc lamps or other incoherent light sources are only of historical interest. Whether the available laser wavelength is suitable for your application depends on the following factors:

- fluorescence
- self-absorption of laser light
- re-absorption of Raman scattered light
- resonance enhancement
- scattering intensity ($\propto \omega^4$, cf. Eq. 1)
- detector, gratings, filters

A second important question you have to ask yourself is what laser power should be used for the measurement. Generally, lasers operate either in continuous wave mode (CW) or in pulse mode. High repetition $kHz - MHz$ pulsed lasers are sometimes referred to as 'quasi CW'. With the exception of time resolved experiments, the signal depends on average power, so there is no advantage to used pulsed lasers if a CW alternative is available. High peak powers from pulsed lasers are rather disadvantageous as they often lead to sample damage or nonlinear effects. For analysis of catalysts by confocal Raman microscopy, laser powers up to 20 mW are typical. For Raman spectroscopy of gases, laser powers up to several watts might be necessary due to the small number density of scatterers.

A word of precaution should be said here. Even 20 mW of laser light can lead to blindness if reflected directly into the eye. At higher powers even stray light can be dangerous. Therefore, protective eye ware should be used when working with lasers and reflective items like rings or watches should be removed. Figure 18 shows the wavelengths covered by the usual Raman shift range ($0-3000\text{ cm}^{-1}$) for

several common laser wavelengths and the quantum efficiency of typical silicon-based CCD detectors. It should be noted that the wavelengths coverage for a given wavenumber range increases with the excitation wavelength.

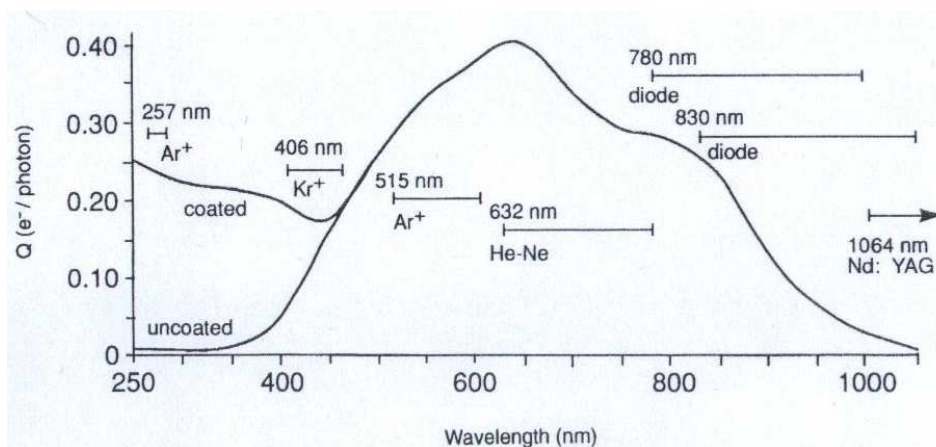


Figure 18: Wavelengths covered by a Raman range of $0 - 3000 \text{ cm}^{-1}$ for several common laser wavelengths. Additionally shown are typical quantum efficiencies of silicon-based CCD detectors. The left end of the bar is the relevant laser wavelength and zero Raman shift. Adopted from [10]

Eq. 37 can be used to calculate the wavelength range for a given maximum wavenumber and laser wavelength.

$$\lambda_{Raman}^{max} = \left(\frac{1}{\lambda_{laser}} - \tilde{\nu}_{max} \right)^{-1} \quad (37)$$

In the Inorganic Chemistry Department two Raman setups exist, a benchtop confocal Raman microscope (LABRAM, Dilor) and a research grade triple spectrometer with confocal microscope (TriVistaCRS, Princeton Instruments). The lasers used with these instruments are a He-Ne laser (632.8 nm) for the LABRAM and an Ar^{+} -laser for the TriVista. The Ar^{+} -laser provides about a dozen wavelengths in the visible range (cf. Fig. 19) with the strongest ones being at 514.5 nm and 488 nm . The 488 nm line is currently used with the TriVista setup, however, the installation of a *UV* laser system for resonance Raman spectroscopy is planned.

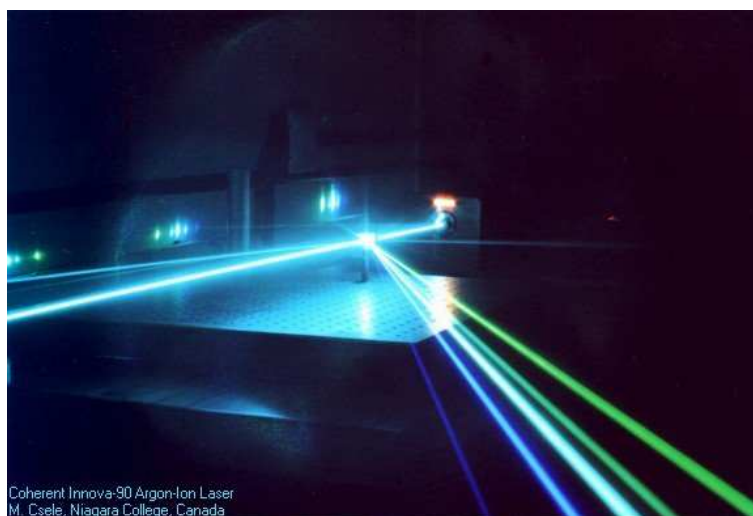


Figure 19: Visible lines of an Ar^+ -laser.

5.2 Sample Illumination

Since Raman spectroscopy is in most cases used as a specialized research technique, a standard way of sample illumination and light collection has not emerged. However, even if the techniques differ in their technical realization, most geometries can be classified as 90° or 180° scattering (Figure 20). In addition to standard collection optics, fiber optic sampling becomes more and more common (Figure 21). For application in heterogeneous catalysis, special in-situ cells with gas flow and temperature control have been developed (Figure 22). Often, sample fluidization or sample rotation is used to minimize sample degradation by the laser light (Figure 22 (a-b)).

5.3 Analysis of the Scattered Light

5.3.1 Dispersive Spectrometer

In both Raman instruments operated in the Inorganic Chemistry Department, dispersive spectrometers are used to analyze the frequency content of the scattered radiation. In both instruments, diffraction gratings accomplish spectral dispersion. Some diffraction gratings and their ruled surface are shown in Figure 23. Low groove density gratings are ruled mechanically (< 1800 *grooves/mm*), high

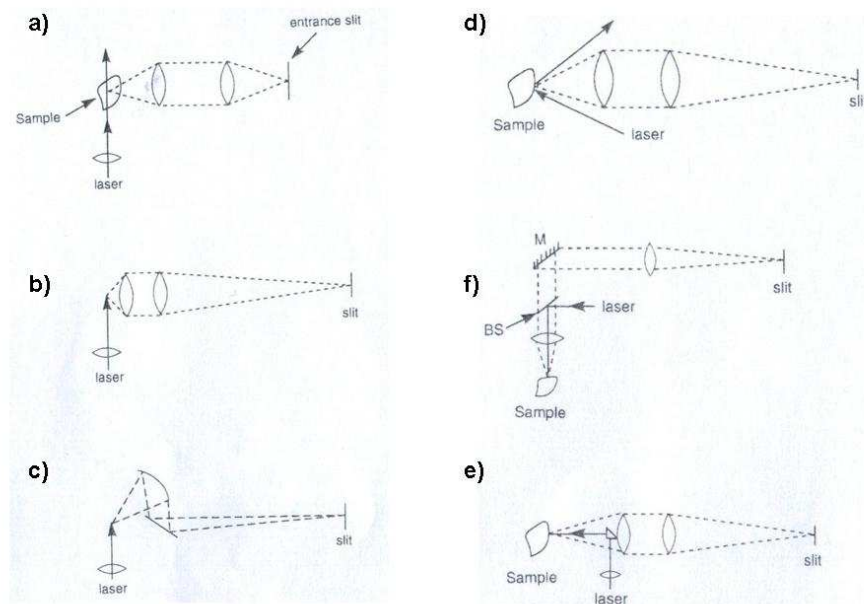


Figure 20: 90 ° (a-c) and 180 ° (d-f) sampling geometries in Raman scattering.

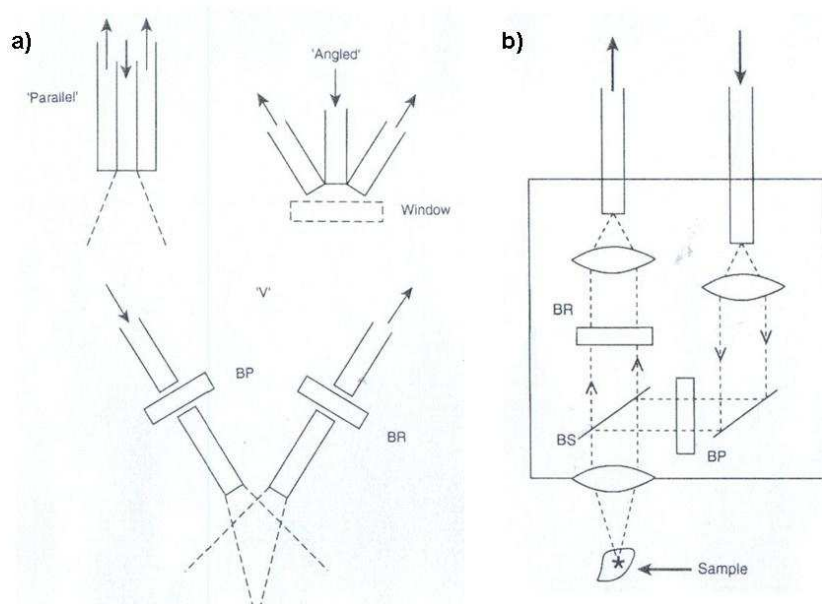


Figure 21: Fiber probes for Raman spectroscopy.

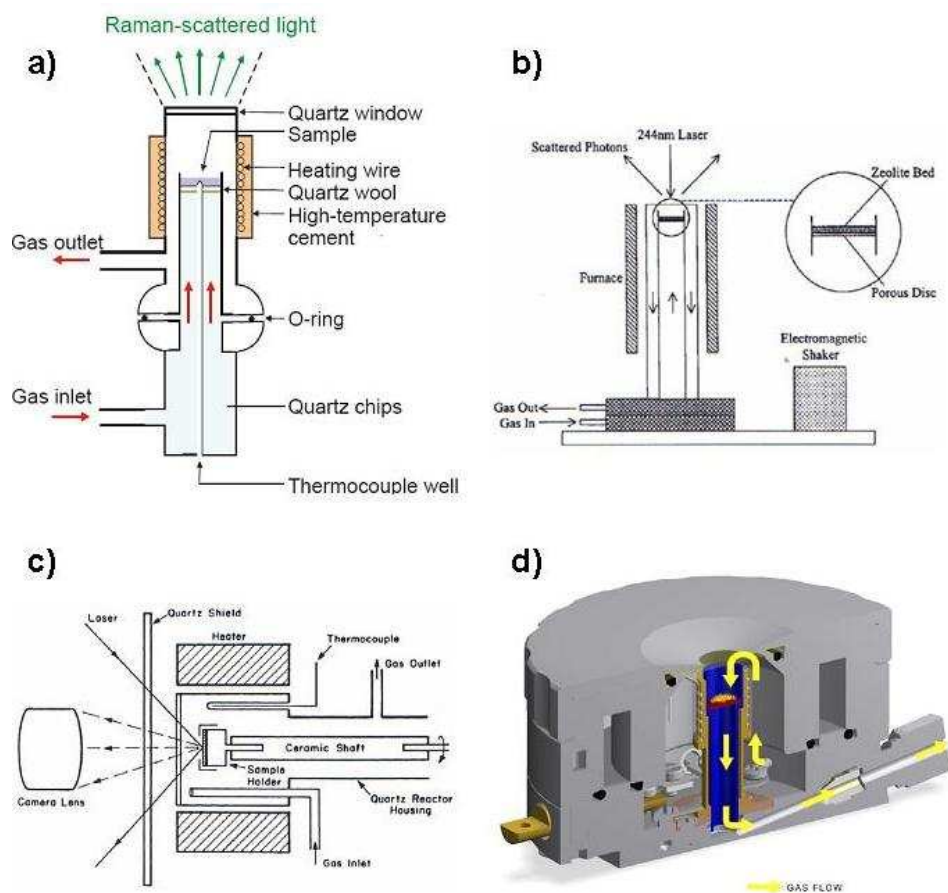


Figure 22: In situ cells for Raman spectroscopy in heterogeneous catalysis.

groove density gratings usually holographically. In the TriVista instrument, each of the three spectrometer stages is built as a so called Czerny Turner spectrometer. This geometry and the corresponding angles are shown in Figure 24. The principle is as follows: After the scattered beam of light passes through the spectrometer entrance slit, it hits a mirror which makes the light parallel (collimating mirror). The collimated light falls on the grating surface at the incident angle α with respect to the grating normal. The grating disperses the incoming light into multiple wavelengths. Each wavelength λ_i is diffracted at a certain angle β_i with respect to the grating normal. The wavelength reaching the center of the CCD chip (or generally your exit slit) is called the central wavelength λ_c . The relation between the central wavelength λ_c , the incident angle α and the diffraction angle β is given by the basic grating equation where m is the grating order (0, 1, 2...) and

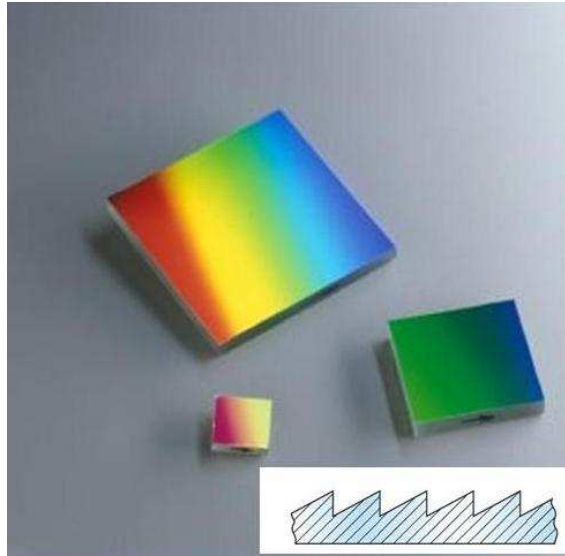


Figure 23: Diffraction gratings as used in dispersive Raman spectroscopy.

N is the groove density (Eq.39):

$$10^{-6} \cdot m \cdot N \cdot \lambda_c = \sin(\alpha) + \sin(\beta) \quad (38)$$

In Czerny Turner geometry, the inclusion angle γ between incoming and outgoing light is constant, hence

$$\gamma = \beta - \alpha \quad (39)$$

If you want now to position a certain wavelength λ_c in the center of your CCD chip, the grating has to be rotated by an angle Ψ which amounts to:

$$\Psi = \arcsin \left(\frac{m \cdot N \cdot \lambda_c}{2 \cdot 10^6 \cdot \cos \left(\frac{\gamma}{2} \right)} \right) \quad (40)$$

If the grating is rotated, the incident angle α and the diffraction angle β of the central wavelength can be calculated from the rotation angle Ψ :

$$\alpha = \Psi - \frac{\gamma}{2} \quad (41)$$

$$\beta = \Psi + \frac{\gamma}{2} \quad (42)$$

In practice you don't have to calculate anything, Eq. 40 is implemented in the software, you just type in the wavelength and the spectrometer rotates the grating accordingly.

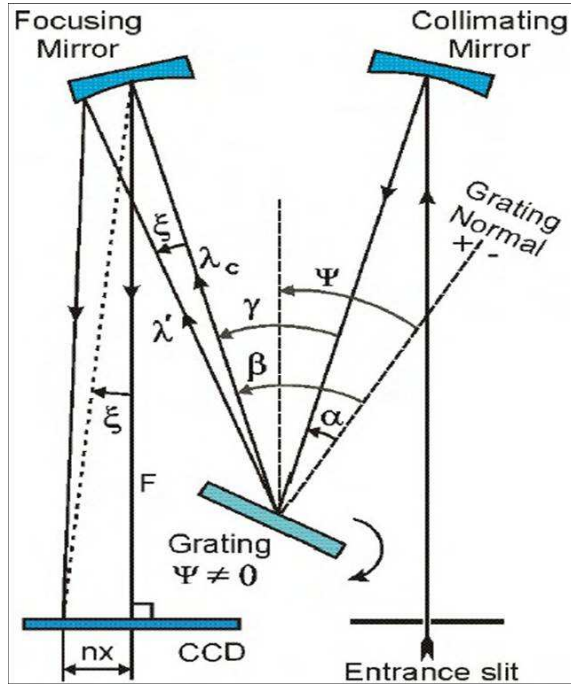


Figure 24: Principle of spectral analysis in the TriVista spectrometer (Czerny Turner geometry).

In the TriVista instrument we operate in lab F2.02a, a CCD camera is used as detector. A CCD chip consists of many small light detection elements called pixels. Our camera uses a chip with 512×2048 pixels. With Eq. 40 it is possible to calculate the central wavelength λ_c that hits the central pixel on the CCD chip. To calculate the spectral coverage of the chip for a given rotation angle Ψ it is necessary to calculate which wavelength λ' hits a pixel in a distance d from the central pixel. If each pixel has the width x , d calculates to:

$$d = n \cdot x \quad (43)$$

with n equals the number of pixels. The diffraction angle for λ' is (cf. 24):

$$\beta' = \beta + \xi \quad (44)$$

The tangent of ξ results from:

$$\tan(\xi) = \frac{n \cdot x}{F} \quad (45)$$

where F is the focal length of the spectrometer (for the TriVista 750 mm). From

Eq. 45, ξ can be calculated:

$$\xi = \arctan\left(\frac{n \cdot x}{F}\right) \quad (46)$$

Plugging Eq. 43-46 into the basic grating Equation 39, λ' can be calculated:

$$\lambda' = \frac{\sin(\alpha) + \sin(\beta')}{10^{-6} \cdot m \cdot N} = \frac{\sin(\alpha) + \sin(\beta + \xi)}{10^{-6} \cdot m \cdot N} = \frac{\sin\left(\Psi - \frac{\gamma}{2}\right) + \sin\left(\Psi + \frac{\gamma}{2} + \arctan\left(\frac{n \cdot x}{F}\right)\right)}{10^{-6} \cdot m \cdot N} \quad (47)$$

Eq. 47 shows that the spectral coverage of your measurement (λ leftmost pixel - λ rightmost pixel) depends inversely on the groove density of the chosen grating N . The higher the groove density, the smaller the wavelength coverage but the higher the spectral resolution and vice versa. It is therefore advisable to use first a low groove density grating (e.g. 500 *grooves/mm*) to measure a low resolution overview spectrum, then select the region of interest and measure it with a high groove density grating (e.g. 2400 *grooves/mm*). For UV measurements, even higher groove density gratings have to be used (e.g. 3600 *grooves/mm*)

5.3.2 Laser Line Rejection

Preceding the spectral analysis, the much more intense elastically scattered Rayleigh light has to be removed. Other words for that are laser line rejection or straylight rejection. In benchtop instruments featuring a single stage for spectral dispersion, this is usually accomplished using either a notch or an edge filter (cf. Fig. 25). Whereas edge filters only allow measuring either the Stokes or Anti-Stokes part

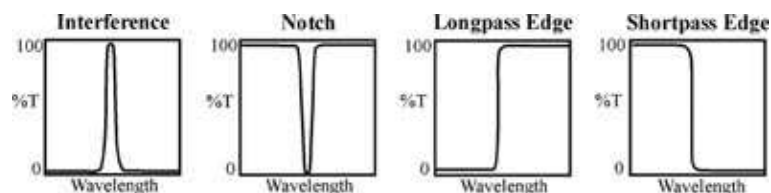


Figure 25: Filter for Raman spectroscopy. Source: www.omegafilters.com

of the spectrum, notch filters allow both and are most often used for Raman spectroscopy. Modern holographic notch filters consist of a photosensitive emulsion in which a sinusoidally varying refractive index profile is imprinted using laser interference patterns. Holographic notch filters allow measurements up to 100 cm^{-1}

to the laser line and have high transmission for all wavelengths outside the band pass. Their disadvantage is that they do not work for wavelengths below 350 nm and that bands close to the laser line can not be measured. Furthermore, as the emulsion is drying out, they have a limited lifetime and changing the excitation wavelengths requires to change the notch filter.

Another way to suppress straylight is using a triple spectrometer in double subtractive mode. The principle is shown in Figure 26. In double subtractive mode

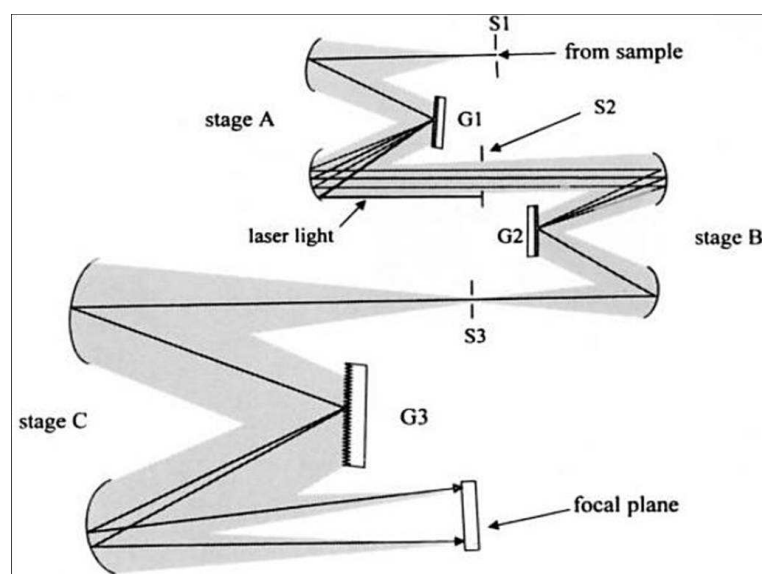


Figure 26: Straylight rejection in double subtractive mode.

the first two spectrometer stages serve as a tunable bandpass filter with variable pass bandwidth providing excellent stray light rejection. With a triple spectrometer working in double subtractive mode, bands as close as 5 cm^{-1} can be measured, a change of excitation wavelength is straightforward and the rejection works also in the UV. Disadvantageous is the low light throughput ($\sim 10\%$) due to multiple gratings and mirrors and the high price. A triple is a versatile spectrometer with excellent stray light rejection but low sensitivity.

5.3.3 Detector

Most Raman spectrometers use charge coupled device detectors (CCD) (Fig. 27). The triumphant advance of the CCD is due to its large dynamic range, low noise

and high quantum efficiency combined with the ability to store and measure charge in two dimensions and hence images. Physically, a CCD is an analogue

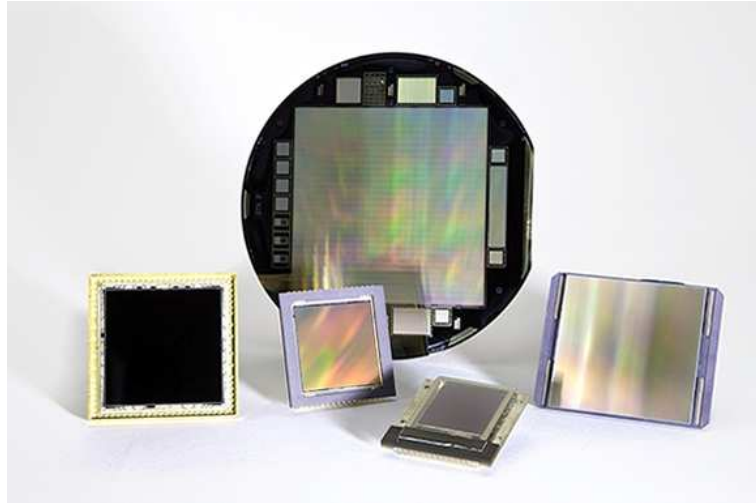


Figure 27: Straylight rejection in double subtractive mode.

shift register that enables the transportation of analogue signals. As the underlying physics are quite complex, simplified models will be used here to illustrate the principle (Fig. 28 and Fig. 29). Very illustrative is the conveyor belt model where each pixel on the CCD chip is imagined as a water bucket. The water buckets are mounted on vertical conveyor belts, each representing a pixel column on the CCD chip. As long as the camera shutter is opened, rain (photons) falls into each bucket which are getting filled during the exposure time more or less. During the readout the vertical conveyor belts transport the water load column by column into readout buckets, mounted on a horizontal conveyor belt which finally empties each bucket into a measuring device (amplifier).

A more physical model is shown in Fig. 29. Most CCD chips consist of two layers of silicon (n-layer and p-layer), covered by a thin insulating SiO_2 layer with electrodes on top. By diffusion of electrons from the n-layer to the p-layer and holes vice versa, an electric field results which separates photoelectrons upon impact of a photon on the silicon and accumulates them just inside the n-layer. To avoid lateral movements, a positive voltage is applied to one of the above laying electrodes, creating a deep potential well with walls formed by the more negative electrons left and right of the positive electrode. During accumulation (shutter

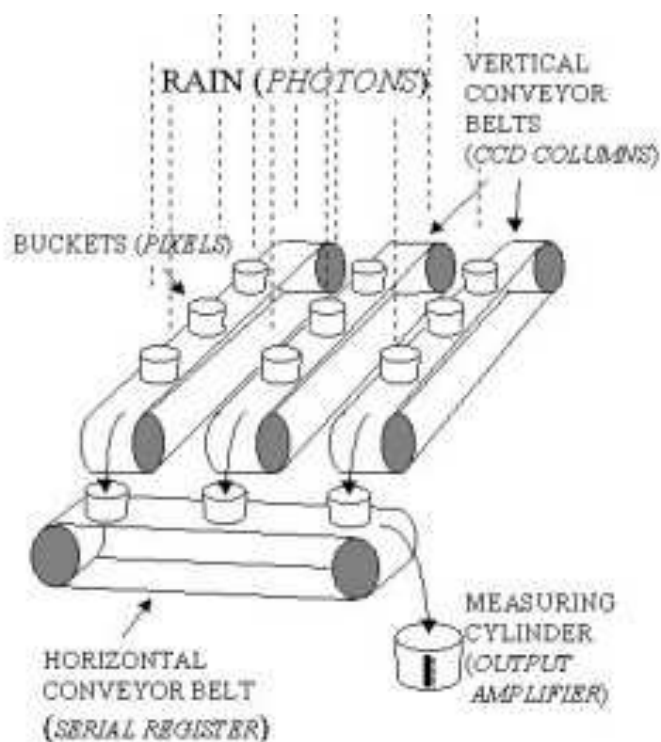


Figure 28: Conveyor model of a CCD chip.

open), photoelectrons fill these wells more or less. For readout, the positive potential and hence the electrons are shifted across the electrode arrangement, i.e. from pixel to pixel (cf. Fig. 29). Due to the bandgap of 1.26 eV , CCD's constructed from silicon are insensitive beyond $1 \mu\text{m}$. For operation in the UV, back illuminated, thinned and UV enhanced CCD's are necessary. For Raman spectroscopy, CCD cooling (electric or liquid N_2) is necessary to minimize thermal noise (dark current).

5.4 Raman Microscopy

Modern Raman spectrometers are often coupled to confocal microscopes to study specimens with high spatial resolution. The confocal scanning microscope was invented by Marvin Minsky in 1955 and patented in 1957. The principle is shown in Fig. 30. In a confocal Raman microscope, the laser beam passes through an aperture and is focused by an objective lens into a small (ideally diffraction limited) focal volume within the sample. The scattered light from the illuminated spot is

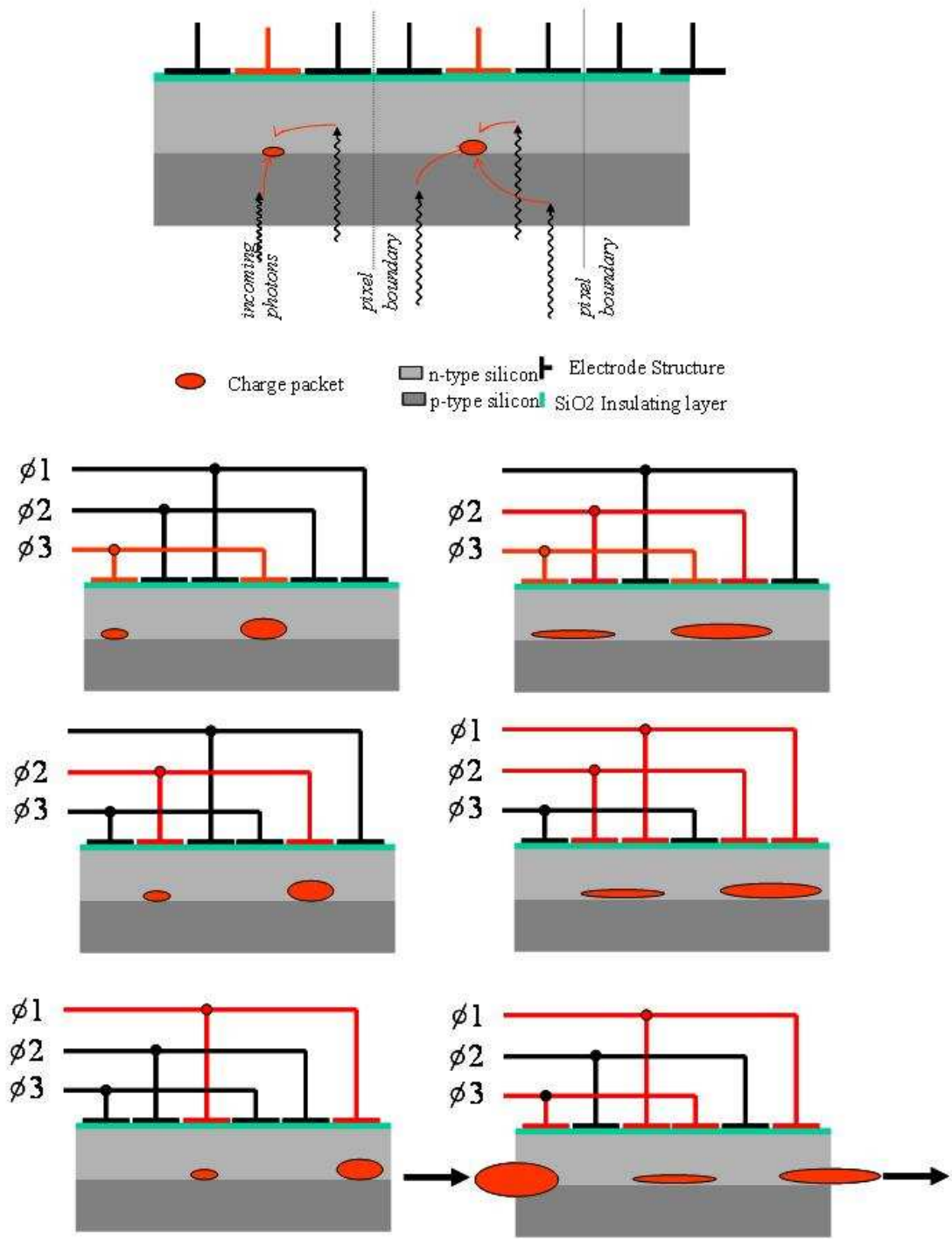


Figure 29: Physical model of a CCD chip.

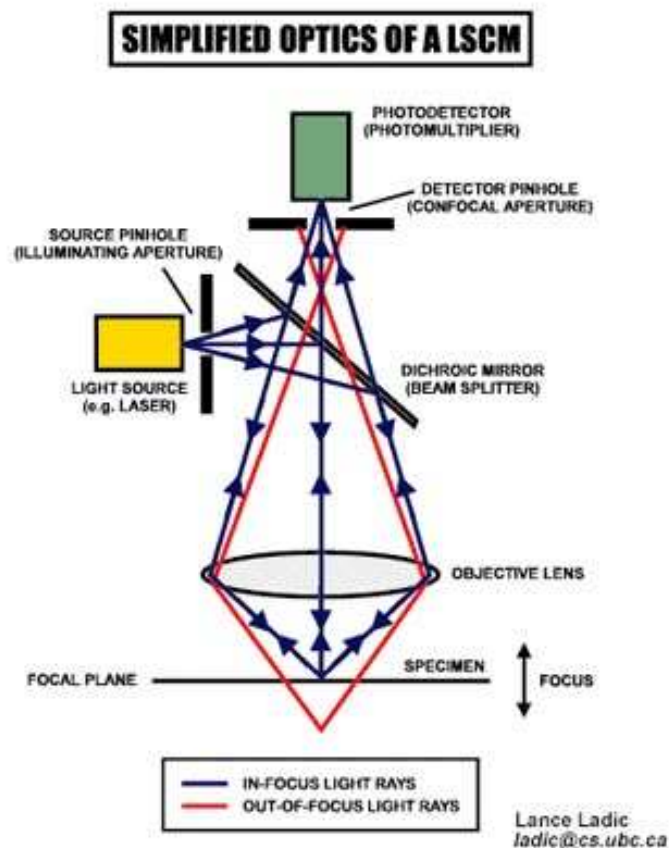


Figure 30: Principle of a confocal Raman microscope.

then recollected by the objective lens in backscattering geometry. After passing a second pinhole, the scattered light is analyzed and detected by the spectrometer as described above.

The high spatial resolution ($< 1 \mu\text{m}^3$) is the result of two effects: i) the laser illuminates only a small volume element in the sample and ii) the detector aperture obstructs the light that is not coming from the focal point. The obvious disadvantage is that only one point can be measured at the time and 2D or 3D images have to be created by scanning the sample in three dimensions using a stepper motor controlled microscope stage.

An application of confocal Raman microscopy is shown in Figure 31 where the reaction



has been followed in a microreactor with channels of $221 \mu\text{m}$ width and $73 \mu\text{m}$

depth [11].

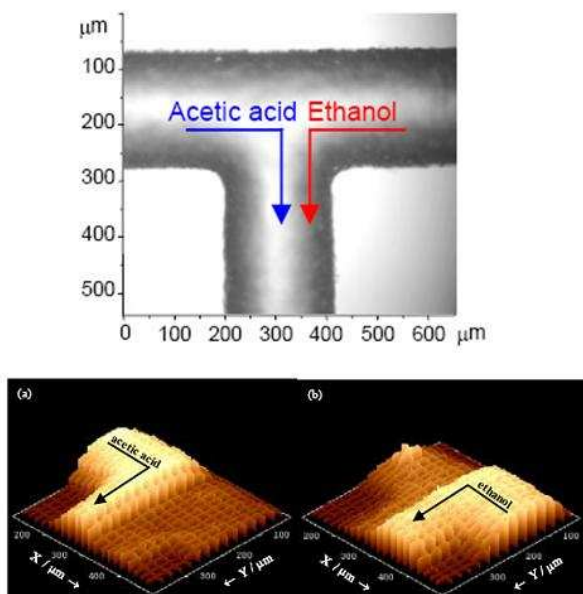


Figure 5: 3D plots of Raman intensity (without background subtraction) in the T-junction region for specific bands. (a) 893 cm^{-1} from acetic acid. (b) 882 cm^{-1} from ethanol.

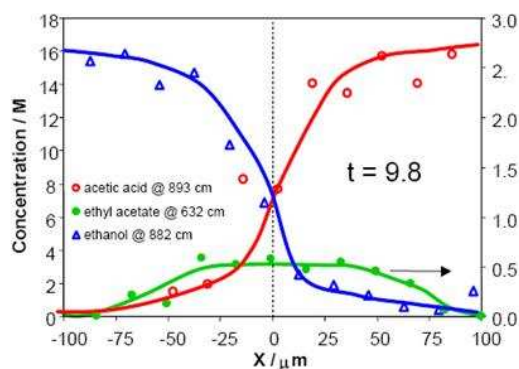


Figure 8: concentration profiles for acetic acid, ethanol and ethyl acetate across the downstream channel at different Y positions, corresponding to 2.3s and 9.8s after initialisation of reaction.

Figure 31: Monitoring of a chemical reaction within a microreactor using confocal Raman microscopy. Adopted from [11].

6 Application of Raman Spectroscopy in Catalysis

6.1 General Comments

Raman spectroscopy has three distinct strengths for application in heterogeneous catalysis: i) it is well suited for in-situ studies as it does not require a probe of any kind, ii) there are no physical boundaries in terms of temperature and pressure and iii) it allows studying surface metal oxide species on typical oxide support materials as SiO_2 , Al_2O_3 , TiO_2 or ZrO_2 . For the latter application, Raman spectroscopy allows studying molecular vibrations below 1100 cm^{-1} like $M = O$,

$M - O - M$ etc. which are obscured in IR because of strong absorption in this spectral range (cf. Fig. 32).

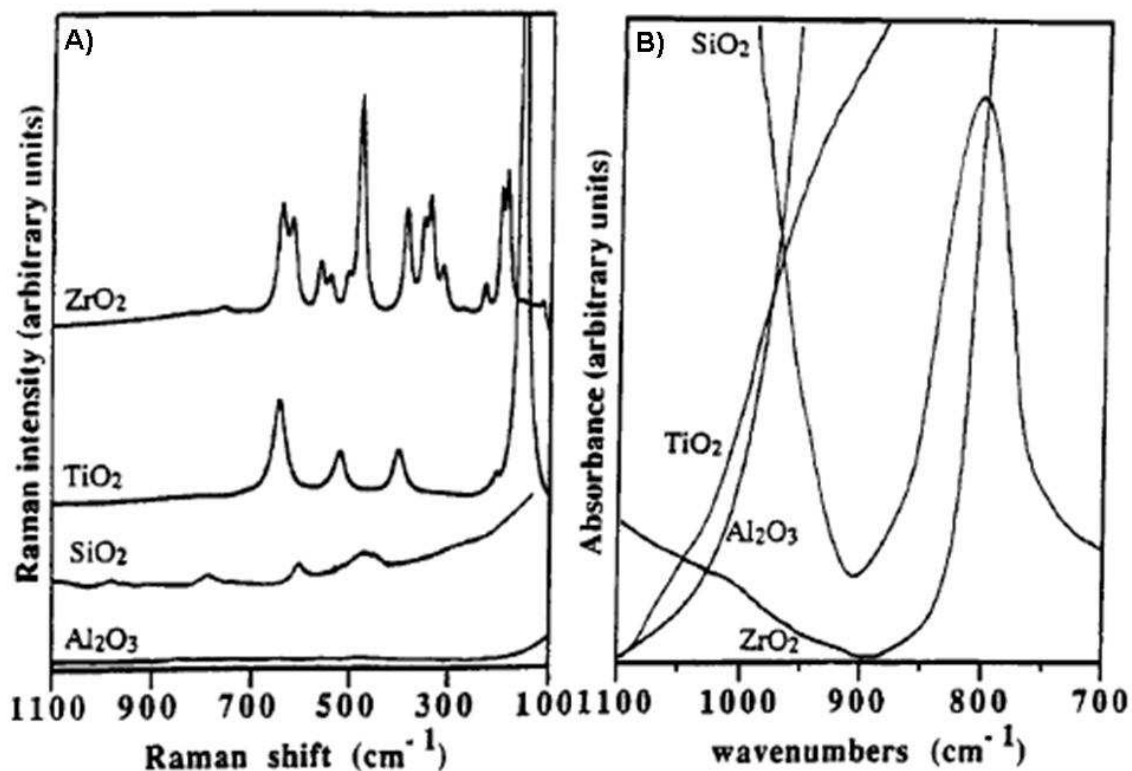


Figure 32: A) Raman spectra of oxide supports (dehydrated at 500 °C) B) Infrared spectra of oxide supports (dehydrated at 500 °C). Adopted from [12].

6.2 Example: Mechanism of NO_2 storage on BaO supported on MgO

As example in this script, how Raman spectroscopy can be applied in heterogeneous catalysis, was taken from the work of C. Hess [13, 14] and concerns the storage mechanism of NO_2 in BaO which is important for automotive exhaust gas clean up. To increase the fuel efficiency of vehicles, engines are developed that work under fuel lean, i.e. oxygen rich conditions. However, excess oxygen leads to enhanced formation of strongly toxic NO_x which needs to be removed from the car exhaust gases. One strategy to accomplish this is NO_x storage-reduction,

where the NO_x is stored in the catalyst under fuel lean conditions and reduced to nitrogen by unburned hydrocarbons under rich conditions.

Raman spectroscopy is well suited to study this system as the covalent $N - O$ bonds in the different NO_x species are good Raman scatterers whereas BaO and MgO are not. Fig. 33 shows how the Raman spectra of a 14 mol% BaO/MgO catalyst change upon flowing 1 % NO in He over it.

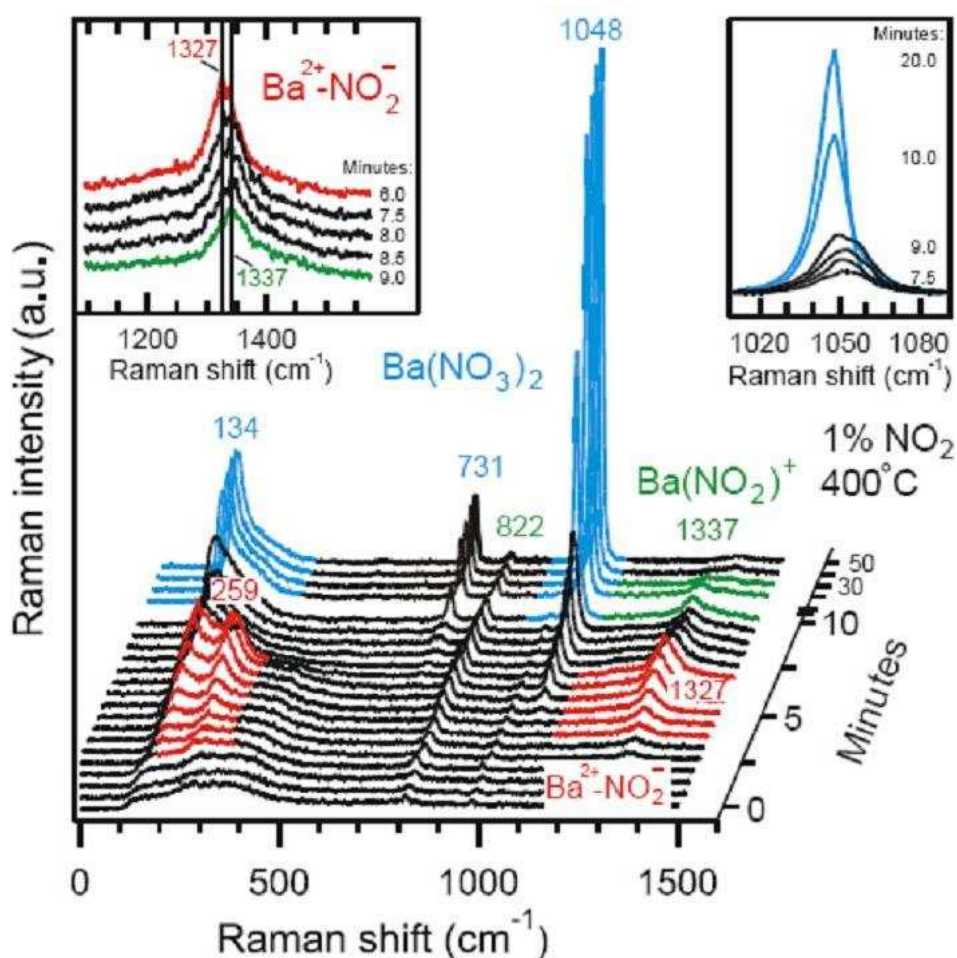


Figure 33: Series of Raman spectra recorded at 40 s intervals of 14 mol% BaO/MgO at 400 °C showing the temporal effect of 1 % NO_2 . Adopted from [13].

Without discussing the details which can be found in [13, 14] the Raman spectra show how NO_2 first binds as a nitro species, i.e. as a ligand coordinated as $Ba^{2+} - NO_2^-$ before it transforms via intermediate stages into crystalline $Ba(NO_3)_2$. Based on this and other in situ Raman experiments as well as supporting results from other techniques (e.g. XRD), Hess could show that the NO_2

storage can be described by the mechanism shown in Fig. 34.

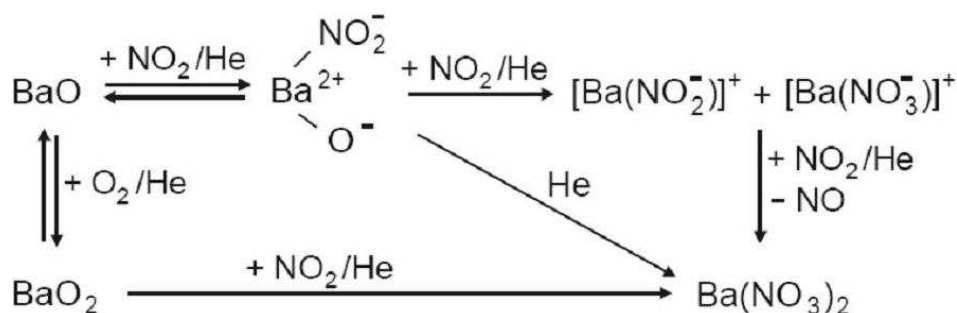


Figure 34: Mechanism of NO_2 storage on BaO as suggested by Hess [13].

References

- [1] Long D. A. *The Raman Effect - A Unified Treatment of the Theory of Raman Scattering by Molecules*. John Wiley & Sons, Ltd, Baffins Lane, Chichester, UK, 2002.
- [2] Smekal A. Zur Quantentheorie der Dispersion. *Die Naturwissenschaften* **1923**, *43*, 873.
- [3] Raman C. V.; Krishnan K. S. A New Type of Secondary Radiation. *Nature* **1928**, *121*, 501.
- [4] Raman C. V.; Krishnan K. S. The Optical Analogue of the Compton Effect. *Nature* **1928**, *121*, 711.
- [5] Landsberg G.; Mandelstam L. A Novel Effect of Light Scattering in Crystals. *Naturwissenschaften* **1928**, *16*, 557.
- [6] Raman C. V.; Krishnan K. S. The Production of New Radiations by Light Scattering. - Part I. *Naturwissenschaften* **1928**, *16*, 557.
- [7] Long D. A. *Raman Spectroscopy*. McGraw-Hill, Inc., 1977.
- [8] Harris D. C.; Bertolucci M. D. *Symmetry and Spectroscopy*. Dover Publications, Inc., New York, 1978.

- [9] Dieterle M. *In Situ Resonance Raman Studies of Molybdenum Oxide Based Selective Oxidation Catalysts*. PhD thesis, Technical University Berlin, 2001.
- [10] McCreery R. L. *Modern Techniques in Raman Spectroscopy*, chapter 2, page 49. John Wiley & Sons, 1996.
- [11] Fletcher P. D. I.; Haswell S. J.; Zhang X. Monitoring of chemical reactions within microreactors using an inverted Raman microscopic spectrometer. *Electrophoresis* **2003**, *24*, 3239.
- [12] Wachs I. E. Raman and IR studies of surface metal oxide species on oxide supports: Supported metal oxide catalysts. *Electrophoresis* **2003**, *24*, 3239.
- [13] Hess C.; Lunsford J. H. Mechanism for NO_2 storage in barium oxide supported on magnesium oxide studied by in situ Raman spectroscopy. *J. Phys. Chem. B* **2002**, *106*, 6358.
- [14] Hess C.; Lunsford J. H. NO storage and reduction in barium oxide supported on magnesium oxide studied by in situ Raman spectroscopy. *J. Phys. Chem. B* **2003**, *107*, 1982.